Novel strengthening mechanism of laser powder bed fusion-manufactured Inconel 718: Effects of customized hierarchical interfaces

Tsuyoshi Mayama [a,*], Takuya Ishimoto [b,c], Masakazu Tane [b], Ken Cho [b], Koki Manabe [b], Daisuke Miyashita [d], Shota Higashino [d], Taichi Kikukawa [b], Hiroyuki Y. Yasuda [b], Takayoshi Nakano [b]

[a] Department of Materials Science and Engineering, Kumamoto University, 2-39-1, Kurokami, Chuo-ku, Kumamoto 860-8555, Japan
[b] Division of Materials and Manufacturing Science, Osaka University, 2-1, Yamadaoka, Suita, Osaka 565-0871, Japan
[c] Aluminium Research Center (ARC), University of Toyama, 3190 Gofuku, Toyama 930-8555, Japan
[d] Graduate School of Engineering, Osaka Metropolitan University, 1-1 Gakuen-cho, Nakaku, Sakai, Osaka 599-8531, Japan

ARTICLE INFO

ABSTRACT

A novel strengthening mechanism involving hierarchical interfaces self-assembled and/or artificially introduced into Inconel 718 (IN718) via laser powder bed fusion (PBF-LB/M) additive manufacturing (AM) has been discovered for the first time. The structures processed by applying two different scanning directions depending on the region have customized hierarchical interfaces that are formed by self-organization of the microscale lamellar structure comprising distinctively different crystal orientations and artificial control of local texture for mesoscale building blocks. The underlying mechanism of strengthening of the structures is clarified using experimental and numerical approaches. Numerical crystal plasticity finite element analysis successfully reproduces the experimental deformation behavior, including the stress-strain curves and anisotropic changes in the shape of the structures, revealing improvements in the mechanical properties by mechanical interaction owing to plastic anisotropy of the lamellar structure. A systematic numerical analysis of the deformation behavior of structures with a higher density of mesoscale interfaces between regions with different local textures suggests possible improvements in the mechanical properties, showing a 13 % increase in 0.2 % proof stress in the optimum structure. Additionally, excellent peak mechanical properties are observed owing to the competition of mechanical interactions between regions with different local textures and a decrease in plastic anisotropy owing to the activation of additional slip modes of the lamellar structure.

1. Introduction

Additive manufacturing (AM) is a promising technology for forming complicated three-dimensional structures [1–6]. Among various AM technologies, the laser-powder bed fusion (PBF-LB/M, which is also frequently referred to as LPBF) technique has attracted considerable attention owing to its superior surface finishing with highly precise building capability than other AM approaches. Recently, a novel technique for controlling the texture of metallic materials using PBF-LB/M AM has been developed [7], wherein a strong single-crystal-like texture is formed depending on the process parameters, including scan strategy. For FCC and BCC metals, the preferential growth direction of the columnar cells is the <100> direction [8]. Under this condition, the crystallographic orientation could be self-adjusted to minimize

misorientations at the melt pool center, where solidification fronts from the right and left halves of the melt pool encounter, realizing the single-crystal-like texture [9]. This technique could open new horizons for metal AM applications. As simultaneous control of shape and crystallographic texture can be achieved using the developed technique, novel applications with controlled local textures can be realized. For example, the local stiffness of structural components such as turbine blades [10] can be optimized by providing different crystallographic textures in each region. Structural components with optimized textures are expected to show significantly improved performance because the different principal stress directions for each region could be different for general non-uniform and/or multi-axial loading conditions. An alternative possible application is in metamaterials comprising multiple building blocks with different crystallographic orientations. Elastic and

---

* Corresponding author.
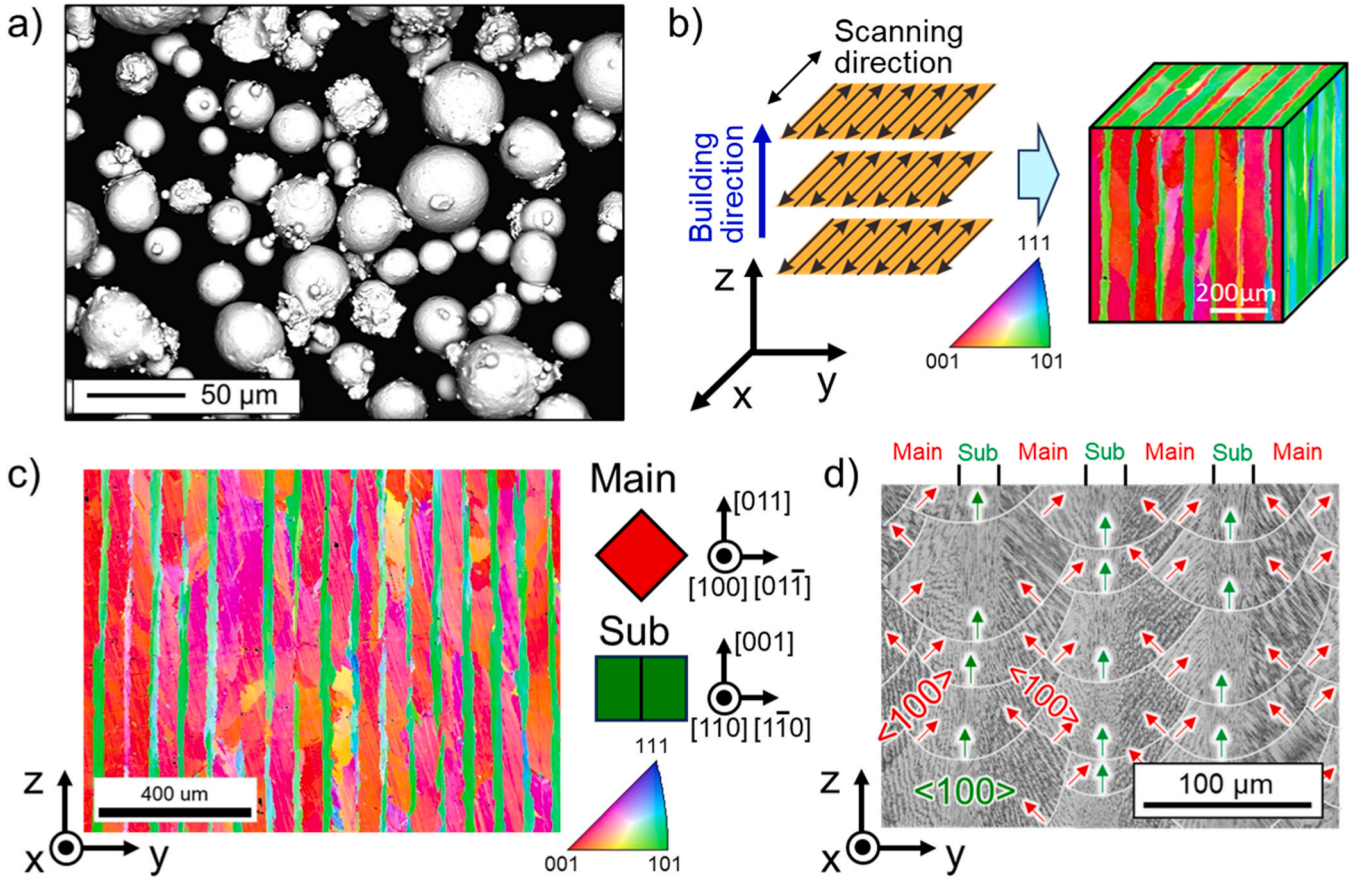*E-mail address:* mayama@kumamoto-u.ac.jp (T. Mayama).

Fig. 1. PBF-LB/M IN718 with self-organized lamellar microstructure. (a) SEM image of spherical powder of IN718. (b) Schematic of crystallographic lamellar microstructure (CLM) formation. (c) Inverse pole figure (IPF) map of lamellar structure. (d) SEM image of cellular microstructure [22].

plastic anisotropies, which predominantly cause the orientation-dependence of the deformation behavior of materials, can lead to mechanical interactions owing to elastic and plastic incompatibility at the interface between different crystal orientations [11–15]. Recent studies on the deformation behavior of oligocrystals have also indicated non-uniform deformation owing to mechanical interaction between several grains [16–19]. While past bicrystal studies have suggested possible modifications to mechanical properties by strong mechanical interactions [20,21], the influence of mechanical interactions on the deformation behavior of multiple grains has not been investigated systematically because the possible combinations are limited owing to difficulties in the fabrication of structures with controlled local texture by conventional processing techniques. Contrarily, the novel texture control technique using PBF-LB/M can enable the production of structures comprising multiple grains with a wide variety of local crystal orientation combinations.

Gokcekaya et al. [22] reported the excellent mechanical properties of a novel PBF-LB/M Inconel 718 (IN718) with a self-organized crystallographic lamellar microstructure (CLM) consisting of two distinctively different crystal orientations. As the microscale lamellar interface is parallel to both the scanning and building directions, a hierarchical structure containing various lamellar interface configurations can be formed by changing the scanning direction according to the region. Although the mechanical properties of the hierarchical structure differ owing to mechanical interactions at interfaces with various combinations of lamellar directions, the deformation behavior of such hierarchical structures can be highly heterogeneous. Therefore, numerical calculations are required to predict the deformation behavior and optimize the hierarchical structure.

The finite element method (FEM) is widely used to analyze and predict the mechanical properties of structures with arbitrary shapes. Although topology optimization of additively manufactured three-dimensional (3D) structures using FEM has been conducted extensively [23–25], conventional FEM with phenomenological constitutive equations that do not consider crystal orientations fails to predict the deformation behavior of materials with strong plastic anisotropy. Conversely, FEM with a crystal plasticity constitutive model [26,27] can reasonably predict the deformation behavior of materials with strong plastic anisotropy because the deformation mechanism at the crystal scale, such as dislocation motion on the slip plane, is explicitly considered as shear strain within continuum mechanics. Therefore, the prediction and exploration of mechanical properties of 3D structures with controlled local textures is possible based on a systematic numerical analysis using FEM with a crystal plasticity constitutive model.

In this study, strengthening of hierarchically structured PBF-LB/M IN718 is achieved by introducing self-organized microscale and artificially introduced mesoscale interfaces. Initially, the elastic and plastic anisotropies of a self-organized microscale lamellar microstructure are experimentally and numerically evaluated. The experimental results of the deformation behavior is numerically reproduced by crystal plasticity FEM analysis, where several slip modes are suppressed owing to mechanical interaction at the microscale lamellar interfaces, causing anisotropic deformation behavior of the lamellar structure. Subsequently, the deformation behaviors of three structures comprising two building blocks with different local textures depending on the scanning direction are examined. Finally, a significant increase in the strength of the multi-story structure is numerically explored using the mechanical interactions of the micro- and mesoscale interfaces. From systematic calculations, the maximum strength of the multi-story structure is determined by a competition between the increase due to mechanical
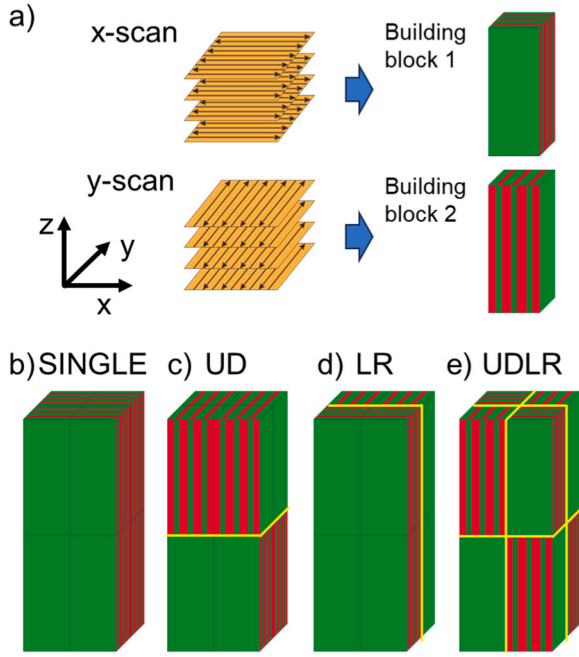
Fig. 2. Hierarchical structures consists of two building blocks. (a) Schematic of two building blocks. (b) SINGLE structure. (c) UD structure. (d) LR structure. (e) UDLR structure. Yellow lines in (c)~(e) indicate interfaces between different building blocks.

interaction at artificially introduced mesoscale interfaces and the decrease due to weakened plastic anisotropy of the lamellar structure owing to the activation of additional slip systems.

2. Experimental and numerical procedures

2.1. PBF-LB/M IN718 with crystallographic lamellar microstructure (CLM)

The fabrication of IN718 specimens is based on a previous study [22]. Specifically, a spherical powder obtained by gas atomization was used for PBF-LB/M with an EOSINT M290 (EOS GmbH Electro Optical Systems), as shown in Fig. 1a. Bidirectional laser scanning was performed along a given axis with a controlled laser power, scan speed, and scan pitch of 360 W, 1000 mm/s, and 80 μm, respectively. Crystallographic lamellar microstructure (CLM) was formed [22], as schematically shown in Fig. 1b. An inverse pole figure (IPF) map obtained by scanning electron microscope (SEM) / electron backscatter diffraction (EBSD) measurements of the CLM is shown in Fig. 1c, where the x- and z-directions correspond to the scanning and building directions (BD), respectively. The lamellar microstructure comprised the main layer and sub-layer with distinctively different crystal orientations. The [100] and [011] directions of the main layer in the crystal coordinate system corresponded to the x- and z-directions, whereas the [110] and [001] directions of the sub-layer corresponded to the x- and z-directions, as schematically illustrated in Fig. 1c. The average width ratio of the main and sub-layers was 7:3 [22]. An SEM image of the cellular microstructure is shown in Fig. 1d, where the arrows indicate the cell elongation directions corresponding to the <100> direction [22]. The regions around the green arrows parallel to BD exhibited crystal orientation of the sub layer, as shown in Fig. 1c. Conversely, the regions around the red arrows, tilting ±45° from BD, exhibited crystal orientation of the main layer. Thus, the main and sub-layers in the CLM were distinguished by their anisotropic cellular structures, as shown in Fig. 1d. Details of the CLM formation mechanism are available in the previous report [22].

2.2. Hierarchical structures comprising two building blocks

Section 2.1 discusses the lamellar microstructure formed by x-directional scanning. Further, a similar fabrication process was applied in the y-direction for the scanning direction in place of the x-direction, and the lamellar structure and crystal orientations were rotated 90° about BD, as schematically illustrated in Fig. 2a. Hereafter, the elementary blocks with lamellar structures constructed by x- and y-scans are referred to as the building blocks in this study. Using the two building blocks, various 3D structures were fabricated by allocating different building blocks from one region to another. Four types of structures comprising 2×2×2 blocks were built for this study, as schematically shown in Fig. 2b–e: SINGLE, UD, LR, and UDLR structures. The SINGLE structure (Fig. 2b) comprised only one type of building block. In the upside–downside (UD) structure (Fig. 2c), different types of building blocks were allocated as upside and downside. For the left–right (LR) structure (Fig. 2d), different types of building blocks were allocated to the left and right regions. In the UDLR structure (Fig. 2e), different types of building blocks were placed alternately. Notably, the UD, LR, and UDLR structures artificially introduced mesoscale interfaces between different building blocks, as indicated by the yellow lines in Fig. 2c–e.

2.3. Measurement of elastic constants

The orthorhombic elastic stiffness components of the present material were experimentally measured using resonant ultrasound spectroscopy (RUS) [28] combined with laser Doppler interferometry (LDI) [29] at room temperature. Two cubic CLM specimens with dimensions of ~4×4×4 mm were cut from the as-processed PBF-LB/M material using a spark-erosion cutting machine. In the RUS analysis, the vibration frequency was swept from 200 kHz to 1.2 MHz to determine the resonance frequencies of the sample. The obtained resonance frequencies were used for LDI analysis to determine the vibration mode of each frequency. From the experimentally measured orthorhombic elastic stiffness, single crystal elastic constants assuming cubic symmetry were identified using an inverse Voigt-Reuss-Hill (iVRH) approximation [30, 31].

2.4. Evaluation of compressive loading behavior

The deformation behavior of the material was experimentally evaluated by compressive loading tests at room temperature. For the compressive loading tests, specimens of dimensions 5×5×12.5 mm were prepared by electrical discharge machining. Uniaxial compressive loading tests were performed with an initial strain rate of 1 % / min. under displacement control.

To specify the active slip modes during compression in the SINGLE structure, slip line analysis was performed. Before compression, the sample surfaces were polished with colloidal silica and were chemically etched for 10 min. using an etchant (HF: HNO$_3$: H$_2$O = 31: 6: 63). After compression, slip lines were observed using a field emission scanning electron microscope (FE-SEM; JSM-6500 F, JEOL).

2.5. Crystal plasticity finite element analysis

Numerical analysis was performed using a static explicit large deformation FEM with a rate-dependent crystal plasticity constitutive model [26]. The {111}<110> slip system of face centered cubic (FCC) metals was implemented in the model. The power-law type equation in Eq. (1) was used to calculate the slip rate for an *i*-th slip system.

$$\dot{\gamma}^{(i)} = \dot{\gamma}_0 \, \text{sgn}(\tau^{(i)}) \left| \frac{\tau^{(i)}}{g^{(i)}} \right|^{1/m} \tag{1}$$

where $\dot{\gamma}_0$, m, and $\tau^{(i)}$ denote the reference slip rate, strain rate sensitivity exponent, and resolved shear stress for the *i*-th slip system, respectively.

Table 1
Definition of twelve slip modes of the {111}<110> slip system.

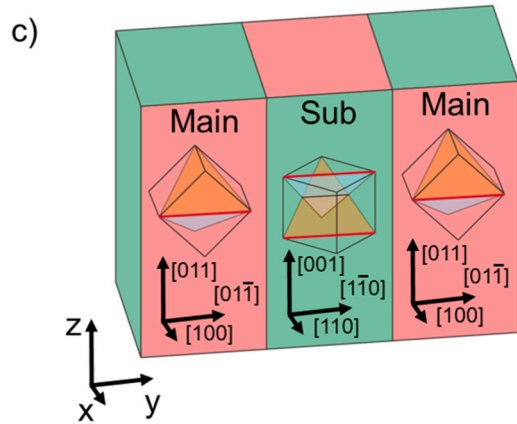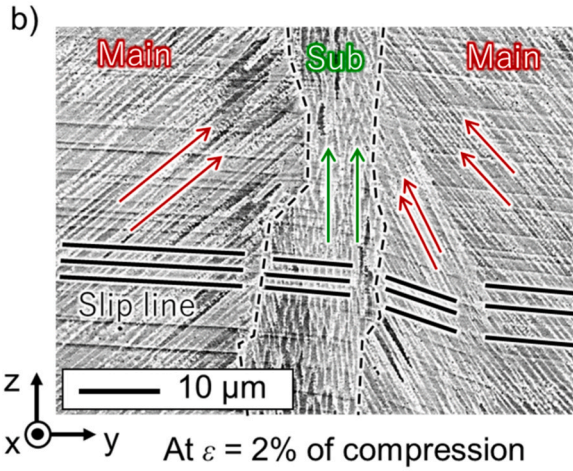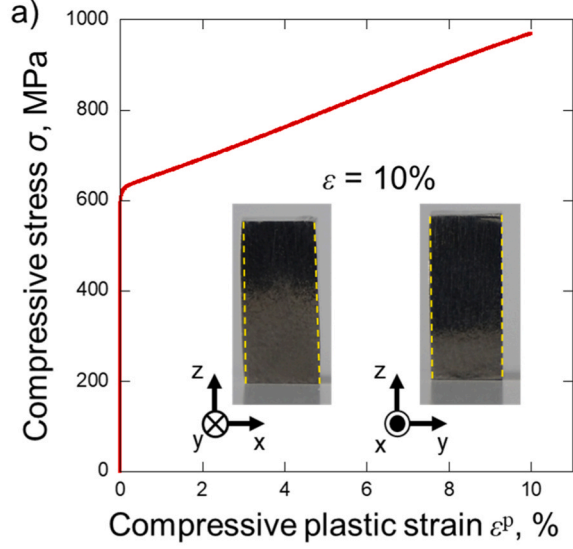| 1	2	3	4	5	6
$(111)[1\bar{1}0]$	$(111)[01\bar{1}]$	$(111)[10\bar{1}]$	$(\bar{1}11)[110]$	$(\bar{1}11)[01\bar{1}]$	$(\bar{1}11)[101]$
7	8	9	10	11	12
$(11\bar{1})[1\bar{1}0]$	$(11\bar{1})[011]$	$(11\bar{1})[101]$	$(1\bar{1}1)[110]$	$(1\bar{1}1)[011]$	$(1\bar{1}1)[10\bar{1}]$

Fig. 3. Experimental results of compressive loading for PBF-LB/M IN718 with CLM (SINGLE structure). (a) Stress-strain curve and deformed shape of specimen after 10 % compression. (b) Backscatter electron image of deformed specimen after 2 % compression. (c) Schematic of possible slip systems for horizontal slip line.

In this study, $\dot{\gamma}_0 = 0.0001$ s^{-1} and $m = 0.02$ were used. In Eq. (1), $g^{(i)}$ represents the reference stress for the *i*-th slip system, which corresponds approximately to critical resolved shear stress (CRSS) when m is close to zero. The hardening law for $g^{(i)}$ was used, as given by Eq. (2).

$$\dot{g}^{(i)} = \sum_j \frac{d\hat{\tau}^{(i)}}{d\Gamma}\Omega^{(ij)}\left|\dot{\gamma}^{(j)}\right| \tag{2}$$

where $\Omega^{(ij)}$ denotes the interaction matrix between slip systems *i* and *j*. In this study, Voce-type hardening law in Eq. (3) was used to calculate $\hat{\tau}^{(i)}$ in Eq. (2).

$$\hat{\tau}^{(i)} = \tau_0^{(i)} + \left(\tau_0^{(i)} + \theta_1^{(i)}\Gamma\right)\left\{1 - \exp\left(-\frac{\theta_0^{(i)}\Gamma}{\tau_1^{(i)}}\right)\right\} \tag{3}$$

where $\tau_0^{(i)}$, $\tau_1^{(i)}$, $\theta_0^{(i)}$, and $\theta_1^{(i)}$ denote the material parameters that describe strain hardening for each slip system. For a detailed discussion on the deformation mechanism based on the crystal plasticity analysis, 12 modes of the {111}<110> slip system were defined, as presented in Table 1.

3. Compressive loading behavior and underlying deformation mechanism of PBF-LB/M IN718 with crystallographic lamellar microstructure (CLM)

3.1. Experimental results

3.1.1. Compressive loading behavior

Fig. 3a shows the relationship between stress and plastic strain of compressive loading tests for PBF-LB/M IN718 with the CLM (SINGLE structure) at room temperature. Similar to the tensile loading behavior observed in previous research [22], PBF-LB/M IN718 with CLM exhibited a high yield stress. After yielding, the stress–strain curve exhibited a nearly linear hardening to ~10 % compression.

The deformed shape of the specimen after compressive loading to a compressive plastic strain of ~10 % is shown in Fig. 3a, wherein observations correspond to the x–z and y–z surfaces. These observations indicate anisotropic changes in the shapes of the specimens. The broken yellow lines in the observed images, which show parallel straight lines on both sides of the specimen, emphasize the change in the specimen shape. The x–z surface shows slight bulging, where the middle part of the specimen expands in the x-direction. Conversely, the y–z surface shows that the side surfaces remain straight after compression, implying that the horizontal expansions in the x- and y-directions are significantly different. In the x-direction parallel to the lamellar interface, a much larger expansion is induced in the lamellar structure.

3.1.2. Slip line observation

A backscattered electron image (BEI) of the sample surface of the SINGLE structure after 2 % compression is shown in Fig. 3b, where the green and red arrows indicate the growth directions of the cells in the main and sub-layers, respectively. The broken lines in Fig. 3b correspond to the lamellar interfaces between the main and sub layers. As indicated by the thick black lines in Fig. 3b, most of the slip lines appear horizontally in both the main and sub-layers. The geometrical relationships between the slip lines and the crystal orientations for each layer are shown in Fig. 3c. The horizontal slip line in the main layer appears due to the activation of the slip system with a slip plane of {111} and/or {1$\bar{1}$ $\bar{1}$}. Contrarily, in the sub-layers, a slip system with a {111} and/or {11$\bar{1}$} slip plane induces a horizontal slip line.

3.2. Crystal plasticity analysis

Crystal plasticity analysis was performed to analyze the underlying mechanism of the experimental results for PBF-LB/M IN718 with the
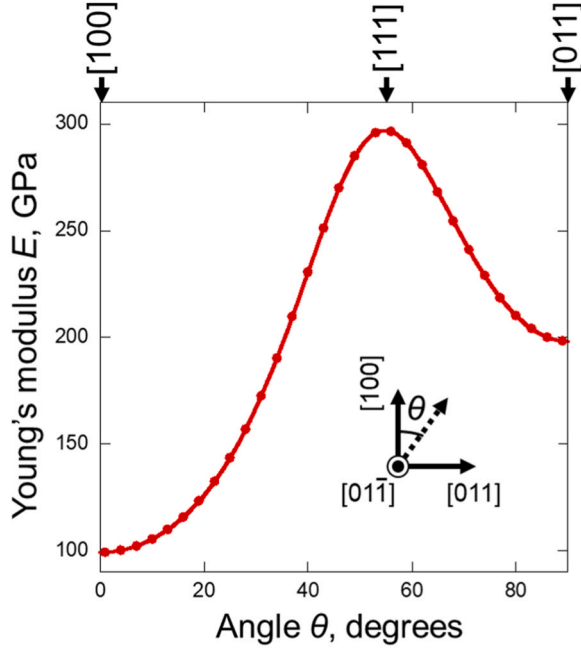
Table 2

Experimentally measured elastic stiffness components of additively manufactured IN718 [GPa].

	c_{11}	c_{22}	c_{33}	c_{12}	c_{13}	c_{23}	c_{44}	c_{55}	c_{66}
Sample 1	239.7	295.8	281.7	139.5	150.0	94.7	50.2	110.6	90.4
Sample 2	238.5	297.4	287.2	142.5	150.5	94.0	49.5	111.3	91.2

Table 3

Estimated elastic stiffness components of the single crystal exhibiting cubic elastic symmetry [GPa].

c_{11}	c_{12}	c_{44}
223.0	152.5	121.8

Fig. 4. Orientation dependence of Young's modulus of single crystal elastic constants which were estimated from experimentally measured elastic stiffness components of additively manufactured IN718.

CLM, as shown in Fig. 3. For realistic calculations, we used the single-crystal elastic constants that were identified based on measurements of the present material, as described in the Section 3.2.1. The material parameters of the Voce-type hardening law in Eq. (3) were identified by fitting the experimental stress–strain curve in Fig. 3a, as described in Section 3.2.2.

3.2.1. Single-crystal elastic constants

Table 2 presents the experimentally measured elastic stiffness values of the two samples of the present PBF-LB/M IN718. Nine independent elastic stiffness components were obtained by assuming orthorhombic elastic symmetry. The difference in stiffness between the two samples was less than 2.2 %, indicating that the measurement method was highly accurate and that the samples were appropriate for the averaged poly-crystal properties. From the nine averaged components of elastic stiffness and Euler angles, which were obtained from the SEM/EBSD analysis of the samples, three independent elastic stiffness components for a single crystal exhibiting cubic elastic symmetry were estimated by the iVRH approximation [30,31], as shown in Table 3.

Although the single-crystal elastic constants are close to previously reported values for the elastic stiffness of IN718 [32–34], the c_{11} and c_{44} values obtained in this study are slightly smaller and higher than the previous values, respectively. The orientation dependence of Young's

modulus as a function of angle θ which is defined by the angle of rotation along [01$\bar{1}$] from [100] to [011], is shown in Fig. 4, where the highest and lowest Young's moduli are 297 and 99 GPa for [111] and [100], respectively. The anisotropy ratio calculated using $2c_{44} / (c_{11} - c_{12})$ is relatively high at 3.455. Thus, the single-crystal elastic constants are used for crystal plasticity analysis.

3.2.2. Calculated compressive loading behavior

Fig. 5a shows the analysis model of the CLM (SINGLE structure) and the boundary conditions for the compressive loading analysis using the crystal plasticity FEM. The initial crystal orientations were set as the ideal orientations for each layer (Fig. 1c). Displacements in all directions of the bottom surface and the x- and y-directions of the top surface were constrained, whereas all the side surfaces were traction-free. An incremental displacement in the negative z-direction was applied to the top surface in accordance with the experimental strain rate of 1 % / min. The material parameters of the Voce-type hardening law in Eq. (3) were identified by fitting the experimental stress–strain behavior of the SINGLE structure. Table 4 lists the material parameters for the analysis.

The stress–strain curves of the experimental and calculated results are presented in Fig. 5b for comparison, where the calculated deformed shape of the specimen after 10 % compression is indicated. The calculated stress–strain curve (solid line) shows good agreement with the experimental results (red symbols). The calculated deformed shape of the specimen qualitatively reproduces the experimental results presented in Fig. 3a. The calculated deformation anisotropy is quantified by induced strain components during compressive loading, as presented in Fig. 5c and d. The relationships between calculated averaged strain components ε_{xx}, ε_{yy}, γ_{xy}, γ_{yz}, and γ_{zx} and the compressive strain are shown in Fig. 5c. Only ε_{xx} shows a continuous increase with compressive strain, thereby indicating significant plastic anisotropy in the present lamellar structure. An enlargement of the early stage of deformation (Fig. 5c) is shown in Fig. 5d. Although deformation up to ~0.3 % is approximately elastic, the strain component shows clear anisotropy (Fig. 5d). While ε_{yy} is induced slightly in Fig. 5d, a much larger increase in ε_{xx} is observed. Hereafter, the model shown in Fig. 5a, which reproduces the experimental deformation behavior of the SINGLE structure, is referred to as the SINGLE model.

3.2.3. Underlying deformation mechanism of the CLM

Fig. 6a shows schematics of the 12 modes of the {111}<110> slip system in the main layer of the SINGLE model. The Schmid factors for each mode are listed in Table 5. In the main layer, slip modes 1, 3, 4, and 6 exhibit the highest Schmid factors of 0.41, while the other eight modes exhibit Schmid factors of zero. The calculated relationship between the average slip rate for each slip mode and the compressive strain in the main layer is presented in Fig. 6b. As anticipated, the four slip modes with the highest Schmid factors are equally activated during compressive loading, whereas the other slip modes show negligible activity (Fig. 6b). Schematics of 12 slip modes in the sub-layer of SINGLE model is shown in Fig. 6c. The Schmid factors for such modes in Table 5 show that slip modes 2, 3, 5, 6, 8, 9, 11, and 12 exhibit the highest Schmid factors of 0.41, whereas the other four modes exhibit Schmid factors of zero. The average slip rate for each slip mode of the sub-layer in Fig. 6d shows that slip modes 5, 6, 11, and 12 are equally activated throughout the compressive loading. Importantly, slip modes 2, 3, 8, and 9 are not activated, although they exhibit the highest Schmid factors, similar to the activated slip modes 5, 6, 11, and 12. The observed results are consistent with the experimental observations in Fig. 3, where only the
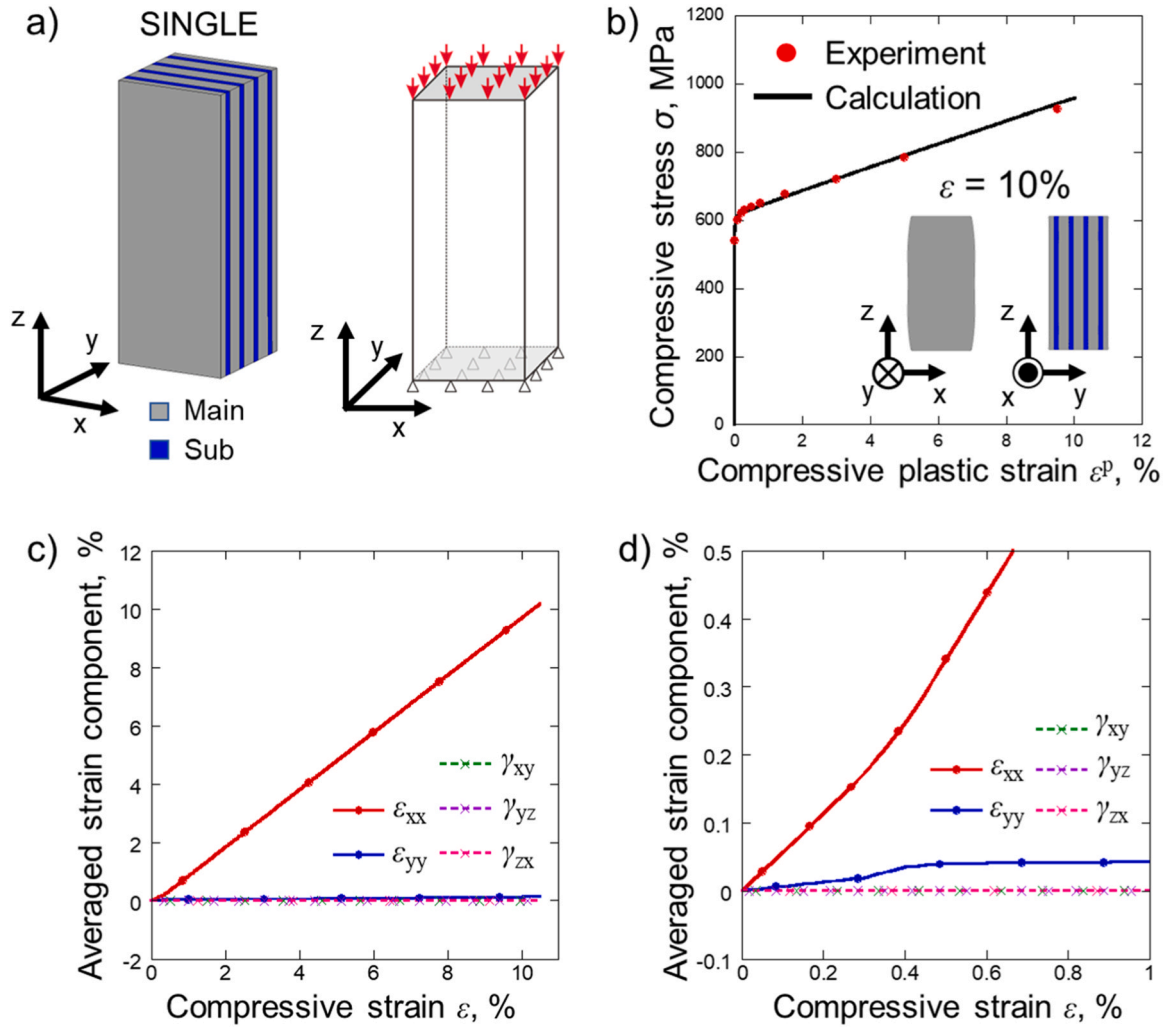
Fig. 5. Calculated results of deformation behavior of the SINGLE structure model. (a) Schematic of analysis model and boundary conditions. (b) Comparison of stress-strain curves between experimental and calculated results, where calculated shape of specimen after 10 % compression is indicated. (c) Relationship between strain components and compressive strain. (d) Enlargement of early stage of deformation shown in (c).

Table 4
Material parameters used in Eq. (3), [MPa].

$\tau_0^{(i)}$	$\tau_1^{(i)}$	$\theta_0^{(i)}$	$\theta_1^{(i)}$
250	1	1000	500

horizontal slip lines are shown in the sub-layer. The suppression of the slip modes in the sub-layer is attributed to the mechanical interaction between the main and sub-layers. Fig. 6e shows distributions of stress component σ_{xx} at a compressive strain of 0.01 %, where only the main or sub-layers are visualized to emphasize the stress distribution on interfaces. When the loading direction is along the z-axis, stress in the x-direction is induced at the interfaces between the main and sub-layers. Compressive and tensile stresses σ_{xx} are induced in the main and sub-layers, respectively. Similarly, compressive and tensile stresses σ_{xx} are induced in main and sub-layers at compressive strain of 10 %, respectively, as shown in Fig. 6f.

The stress in the x-direction (Fig. 6e and f) can be reasonably explained as resulting from elastic and plastic anisotropies. The mechanical interaction between the main and sub-layers is induced owing to the difference in the strain components during compression. For elastic deformation of a single crystal with main and sub-layer orientations, the third column of the elastic compliances in the sample

coordinates exhibits the strain component ratios that are induced during uniaxial loading in the z-direction. The elastic compliances for the main layer and sub-layer in the sample coordinates were calculated by using the elastic stiffness presented in Table 3 and the transformation matrix for stresses or strains in the matrix form [35]. The detailed procedure for the present material is described in Supplementary Note 1.

$$[S_{\mathrm{main}}] = \begin{pmatrix} 1.0085 & -0.41 & -0.41 & 0 & 0 & 0 \\ -0.41 & 0.5047 & 0.0943 & 0 & 0 & 0 \\ -0.41 & 0.0943 & 0.5047 & 0 & 0 & 0 \\ 0 & 0 & 0 & 2.8361 & 0 & 0 \\ 0 & 0 & 0 & 0 & 0.8209 & 0 \\ 0 & 0 & 0 & 0 & 0 & 0.8209 \end{pmatrix} \left[10^{-2}/\mathrm{GPa}\right]$$

(4)

$$[S_{\mathrm{sub}}] = \begin{pmatrix} 0.5047 & 0.0943 & -0.41 & 0 & 0 & 0 \\ 0.0943 & 0.5047 & -0.41 & 0 & 0 & 0 \\ -0.41 & -0.41 & 1.0085 & 0 & 0 & 0 \\ 0 & 0 & 0 & 0.8209 & 0 & 0 \\ 0 & 0 & 0 & 0 & 0.8209 & 0 \\ 0 & 0 & 0 & 0 & 0 & 2.836 \end{pmatrix} \left[10^{-2}/\mathrm{GPa}\right]$$

(5)

On normalizing the third column of Eq. (4) by $[S_{\mathrm{main}}]_{33}$, ε_{xx} and ε_{yy} under $\varepsilon_{zz} = 1$ for the main layer are -0.812 and 0.187, respectively. Similarly, on normalizing the third column of Eq. (5) by $[S_{\mathrm{sub}}]_{33}$, ε_{xx} and
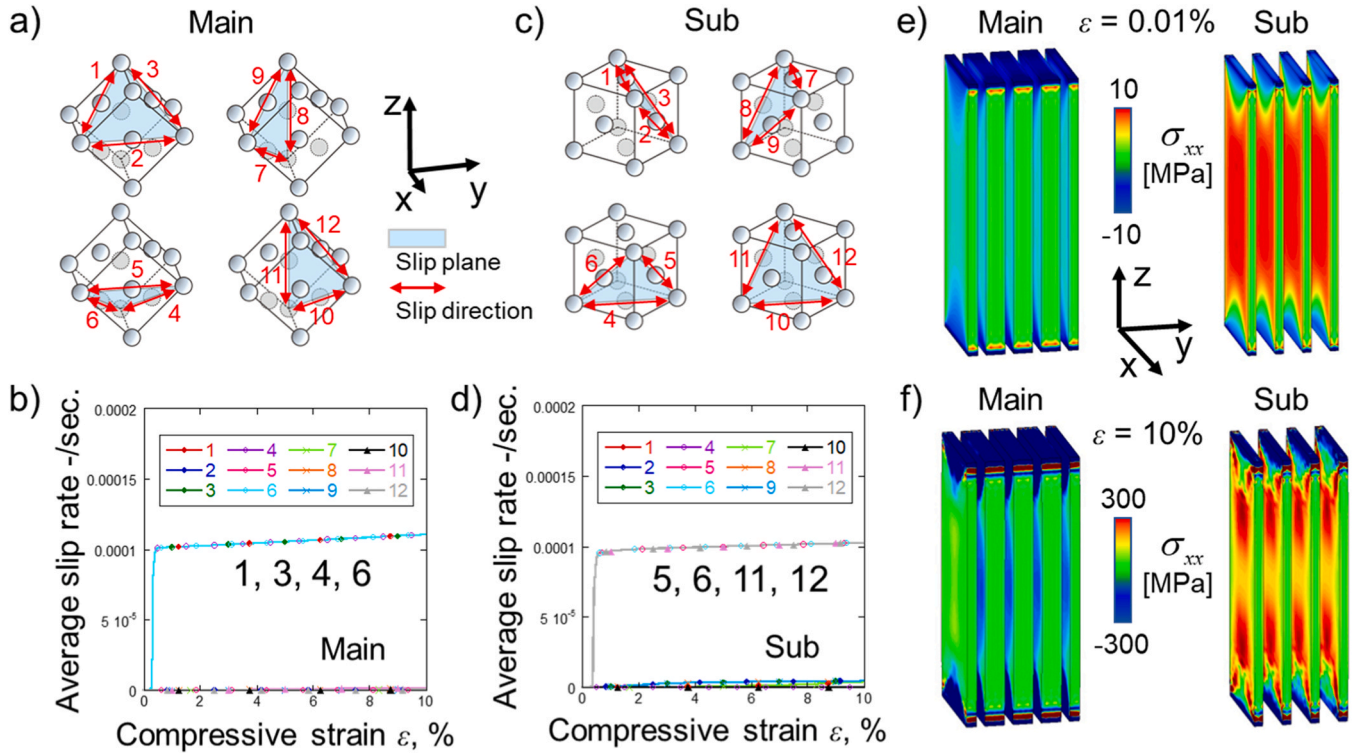
Fig. 6. Deformation mechanism of the lamellar structure. (a) Definition of slip system in the main layer. (b) Calculated activity of slip system in the main layer. (c) Definition of slip system in sub layer. (d) Calculated activity of slip system in the sub layer. (e) Calculated distributions of stress component xx (σ_{xx}) at a compressive strain of 0.01 %. (f) Calculated distributions of stress component xx (σ_{xx}) at a compressive strain of 10 %.

Table 5
Schmid factors for z-directional loading.

No.	1	2	3	4	5	6	7	8	9	10	11	12
Main	0.41	0.00	0.41	0.41	0.00	0.41	0.00	0.00	0.00	0.00	0.00	0.00
Sub	0.00	0.41	0.41	0.00	0.41	0.41	0.00	0.41	0.41	0.00	0.41	0.41

ε_{yy} under $\varepsilon_{zz} = 1$ for the sub-layer are -0.407 and -0.407, respectively. Thus, the elastic deformation of the main layer is strongly anisotropic in the x–y plane, whereas the sub-layer shows isotropic elastic deformation in the x–y plane during compression in the z-direction. The difference in the elastic anisotropies induces mechanical interactions between the main and sub-layers. As a consequence of elastic mechanical interaction,
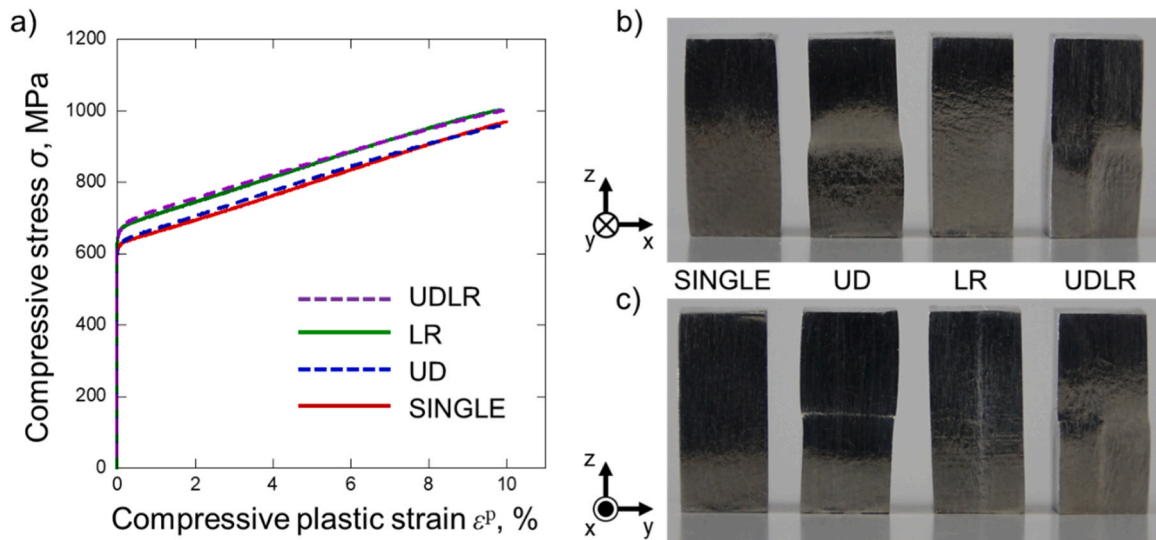

Fig. 7. Experimental results of deformation behavior in the hierarchical structure of PBF-LB/M IN718. (a) Stress-strain curves. Observation of a change in the shape of specimens after compression to ~10 % on the (b) x–z surface and (c) y–z surface.

the SINGLE model comprising a single building block exhibits significant elastic anisotropy (Fig. 5d), where ε_{xx} is predominantly induced during compression in the z-direction from the beginning of deformation.

Considering elastic–plastic deformation, the main layer shows a strong anisotropic deformation, whereas the deformation of the sub-layer is isotropic, as discussed in Supplementary Note 2. The strong anisotropy originates from the suppression of slip modes 2, 3, 8, and 9, as mentioned above. The suppression of slip modes 2, 3, 8, and 9 in the sub-layer causes a strong plastic anisotropy in the sub-layer, because the activities of slip modes 5, 6, 11, and 12 induce tensile plastic strain only in the x-direction during compressive loading in the z-direction. The activated slip modes 1, 3, 4, and 6 in the main layer, as shown in Fig. 6b, induce tensile plastic strain only in the x-direction, similar to the case of a single crystal with a main layer orientation, as shown in Supplementary Note 2. Consequently, reflecting the plastic anisotropies of the main and sub-layers, the SINGLE model comprising a single building block exhibits strong plastic anisotropy, as shown in Fig. 5c. Strong plastic anisotropy leads to plastic incompatibility at the interface between different building blocks, thereby modifying the mechanical properties, as reported in previous bicrystal studies [20,21] and as discussed in Section 4.

4. Strengthening by introduction of meso-scale interfaces

4.1. Experimental results of hierarchically structured PBF-LB/M IN718

The relationships between stress and plastic strain during compressive loading tests for the SINGLE, UD, LR, and UDLR structures at room temperature are shown in Fig. 7a. The deformation behavior depends on the structure. Compared to that of the SINGLE structure, the flow stress levels of the UDLR and LR structures are significantly higher, whereas the UD structure exhibits only a slight increase in the flow stress level. The UDLR and LR structures show equally higher yield stresses than the SINGLE and UD structures. After yielding, the stress–strain curves of all structures show nearly linear hardening up to 10 % plastic strain in compression.

The deformed shapes of the specimens after compressive loading to a compressive strain of ~10 % are shown in Fig. 7b and c, which present observations of the x–z and y–z surfaces of the deformed specimens, respectively. The observations indicate anisotropic changes in the shapes of the specimens. Particularly, the UD structure exhibits a large horizontal expansion on the lower side in Fig. 7b, whereas the horizontal expansion is much larger on the upper side in Fig. 7c. The anisotropic change in shape, which depends on the region in each structure, is reflected by the anisotropy of the CLM, as shown in Figs. 3 and 5.

This study focuses on hierarchical interfaces self-assembled and/or artificially introduced into IN718 via PBF-LB/M and their contribution to the strength of IN718. However, since IN718 is generally used after heat treatment for solutionization and aging, the effects of heat treatment must also be considered. A standard heat treatment with this alloy described in Supplementary Note 3 [36] was conducted on the UDLR structure that showed the highest strengths in the as-built condition (Fig. 7a). After heat treatment, the characteristic CLM was maintained without collapsing owing to grain growth and/or recrystallization (Fig. S2a), indicating the high thermal stability of the microstructure with hierarchical interfaces. Furthermore, owing to the persistence of the hierarchical interfaces, the anisotropic deformation behavior similar to that observed in the as-built specimen was also maintained (Fig. S2b). The 0.2 % proof stress was more than twice that of the as-built specimen (over 1300 MPa) indicating significant strengthening owing to precipitation of the strengthening phases (γ' and γ'') [36]. Based on this peculiar deformation behavior, a similar relative strength relationship after heat treatment as in the as-built condition is assumed, but should be clarified in future studies.
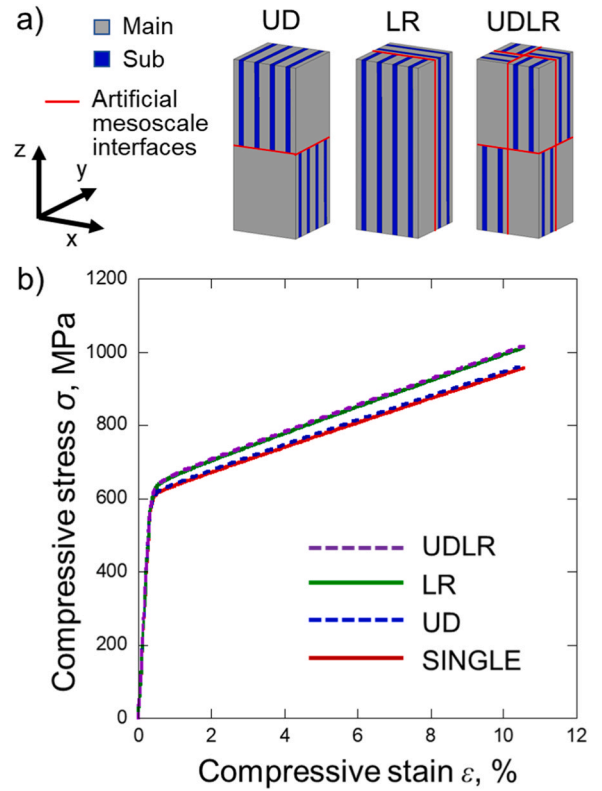

Fig. 8. Calculated results of the deformation behavior of AM structures comprising two building blocks. (a) Schematic of UD, LR, and UDLR structure models. (b) Calculated stress-strain curves of AM structures.

Table 6
Calculated mechanical properties of each model.

Model	SINGLE	UD	LR	UDLR
Young's modulus E, GPa	186.80	187.84	187.87	187.95
0.2 % proof stress σ_Y, MPa	617.20	618.81	636.61	638.55
Strain hardening $\sigma_{10\%} - \sigma_Y$, MPa	322.17	327.71	357.15	359.45

4.2. Crystal plasticity analysis for hierarchical structures

4.2.1. Analysis models

In this section, the elastic and plastic deformation behaviors of the hierarchical structures in Fig. 2c–e are numerically examined using crystal plasticity FEM. The analysis models of each structure are shown in Fig. 8a, where the gray and blue regions correspond to the main and sub-layers, respectively. Red lines in the schematic show interfaces between different building blocks, which are referred to as "mesoscale interfaces" in this study. Each block is modelled using two sub-layers sandwiched between the main layers. For this study, the volume fractions of the main and sub-layers are set as 70 and 30 %, respectively, in accordance with the actual lamellar structure shown in Fig. 1. The influence of the number of layers within a block is presented in Supplementary Note 4.

4.2.2. Calculated compressive loading behavior

Fig. 8b shows the calculated stress–strain curves which were derived from the applied displacement at the top surface of the model and the total nodal force at all nodes on the top surface. The calculated flow stress levels differ significantly depending on the model. The UDLR and LR models exhibit equally higher flow stress levels than the UD and
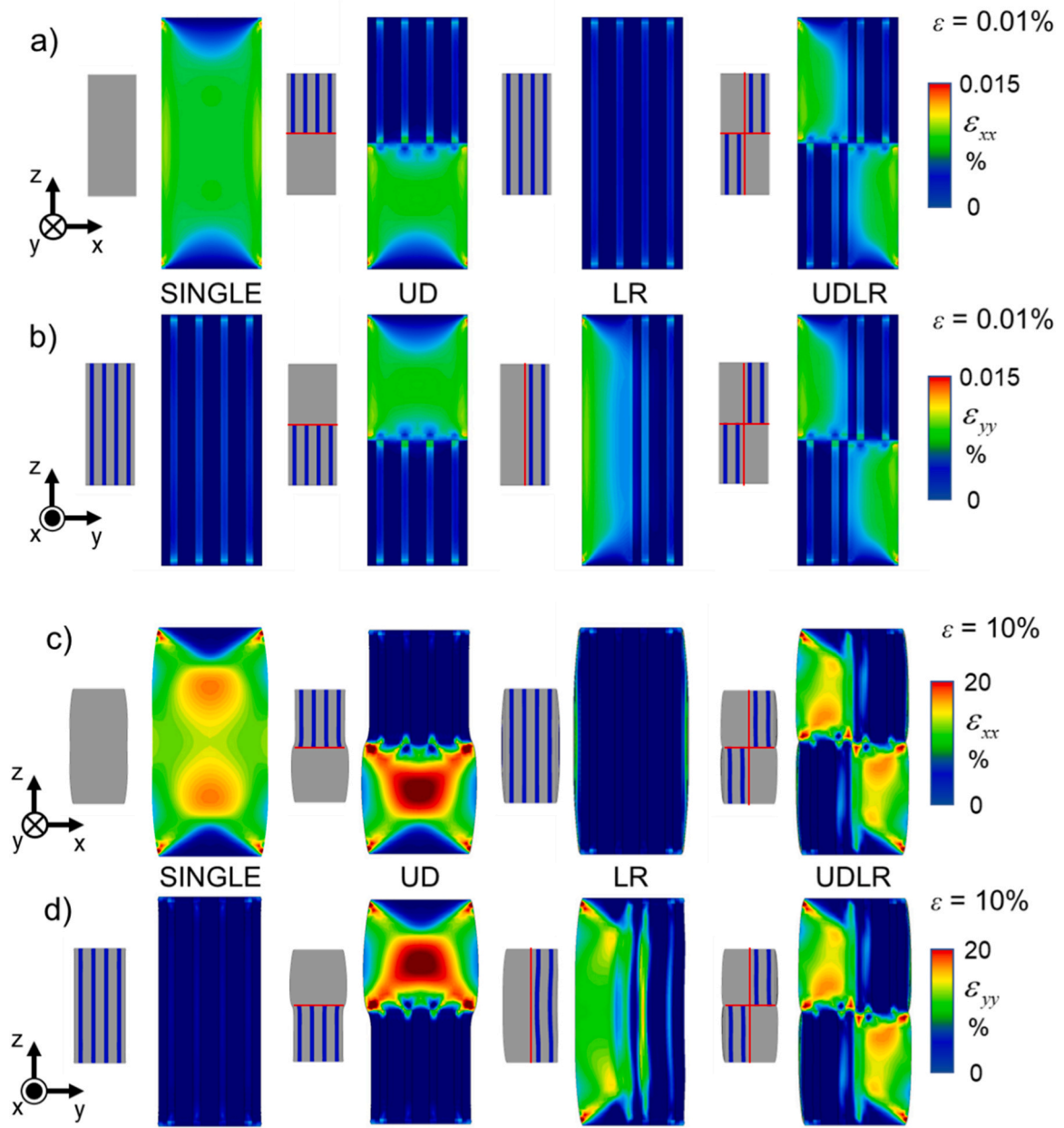
Fig. 9. Calculated distribution of strain components xx ($\varepsilon_{\mathrm{xx}}$) and yy ($\varepsilon_{\mathrm{yy}}$) in AM structures after (a, b) 0.01 % compression and (c, d) 10 % compression, where the deformed shape of the specimens is indicated.

SINGLE models, which is in good agreement with the experimental results shown in Fig. 7a. From the calculated stress–strain curves in Fig. 8b, the Young's modulus, 0.2 % proof stress, and the amount of strain hardening from yielding to a compressive strain of 10 % for each model are calculated. Table 6 lists the computed data. The Young's modulus is derived from the nominal stress and nominal strain at a compressive strain of 0.01 %. The 0.2 % proof stress is calculated using the calculated stress, strain, and Young's modulus for each model. For this study, the amount of strain hardening is defined as the increase in compressive stress from the yield strain, which denotes the strain at a plastic strain of 0.2 %, to a compressive strain of 10 %. As shown in Table 6, the Young's modulus, 0.2 % proof stress, and strain hardening depend on the structure. Compared to the Young's modulus of the SINGLE model, those of the other models exhibited slightly higher values. Particularly, the UDLR model exhibits the highest Young's modulus. The volume fractions of each layer are identical for all models. Therefore, all models have the same volume fraction of regions where

the [011] or [001] loading is applied. Consequently, the difference in Young's moduli presented in Table 6 can be attributed to the artificially introduced mesoscale interfaces between the building blocks. While the difference of Young's modulus in Table 6 is small, this difference is much larger than a computational error. The calculations with the isotropic elasticity in Supplementary Note 5 reveal that Young's modulus of all the models are exactly the same.

4.2.3. Underlying deformation mechanism

The elastic and plastic deformation behaviors of the AM structure comprising two building blocks exhibit clear differences depending on the structure, as shown in Table 6 and Figs. 7 and 8. To understand the structural dependence, the underlying deformation mechanisms of the constituent building blocks are discussed in detail.

The calculated distributions of ε_{xx} and ε_{yy} in all models at a compressive strain of 0.01 % are shown in Fig. 9a and b, where plastic deformation is negligibly small (A negligibly small plastic strain is

Table 7
Calculated total strain energy [Nm].

Model	SINGLE	UD	LR	UDLR
0.01 %	2.873×10^{-4}	2.908×10^{-4}	2.907×10^{-4}	2.911×10^{-4}
10 %	15.90	16.16	16.79	16.88

induced even at a small stress other than zero when the rate-dependent equation in Eq. (1) is used.) Beside each distribution, the calculated results of the deformed lamellar structure are indicated for reference to the configurations of each layer, where the gray and blue regions correspond to the main and sub-layers, respectively. In the SINGLE model, much larger strain ε_{xx} is induced in Fig. 9a whereas only negligibly small strain ε_{yy} is induced in Fig. 9b. Thus, the deformation of the lamellar structure exhibits a strong anisotropy. Accordingly, during compression in the z-direction, the expansion parallel to the lamellar interfaces in the x-direction is quite large, whereas almost no thickness change occurs normal to the lamellar interfaces.

The calculated distributions of ε_{xx} and ε_{yy} at a compressive strain of

10 % are shown in Fig. 9c and d, respectively. The strain distributions are qualitatively similar to those at a compressive strain of 0.01 %, as shown in Fig. 9a and b. Furthermore, similar to the experimental observations in Fig. 7b and c, the changes in the shape of the specimens show significant differences depending on the structure. In the SINGLE model, large strain ε_{xx} is induced (Fig. 9c), whereas only a negligibly small strain ε_{yy} is induced, as shown in Fig. 9d. Thus, the deformation of the lamellar structure exhibits strong anisotropy. The anisotropic deformation behavior of the building block explains the strain distributions of all the models in Fig. 9c and d. For instance, the lower region of the UD model indicates a large expansion in the x-direction parallel to the lamellar interfaces, as shown in Fig. 9c. Contrarily, the upper region of the UD model shows significant expansion in the y-direction, which is parallel to the lamellar interfaces (Fig. 9d). The influence of elastic anisotropy on the deformation behavior of the lamellar structure consisting of the main and sub-layers is discussed in Supplementary Note 5.

Mechanical interactions at the mesoscale interfaces between different building blocks owing to elastic and plastic anisotropies, as mentioned above, cause modifications in the mechanical properties
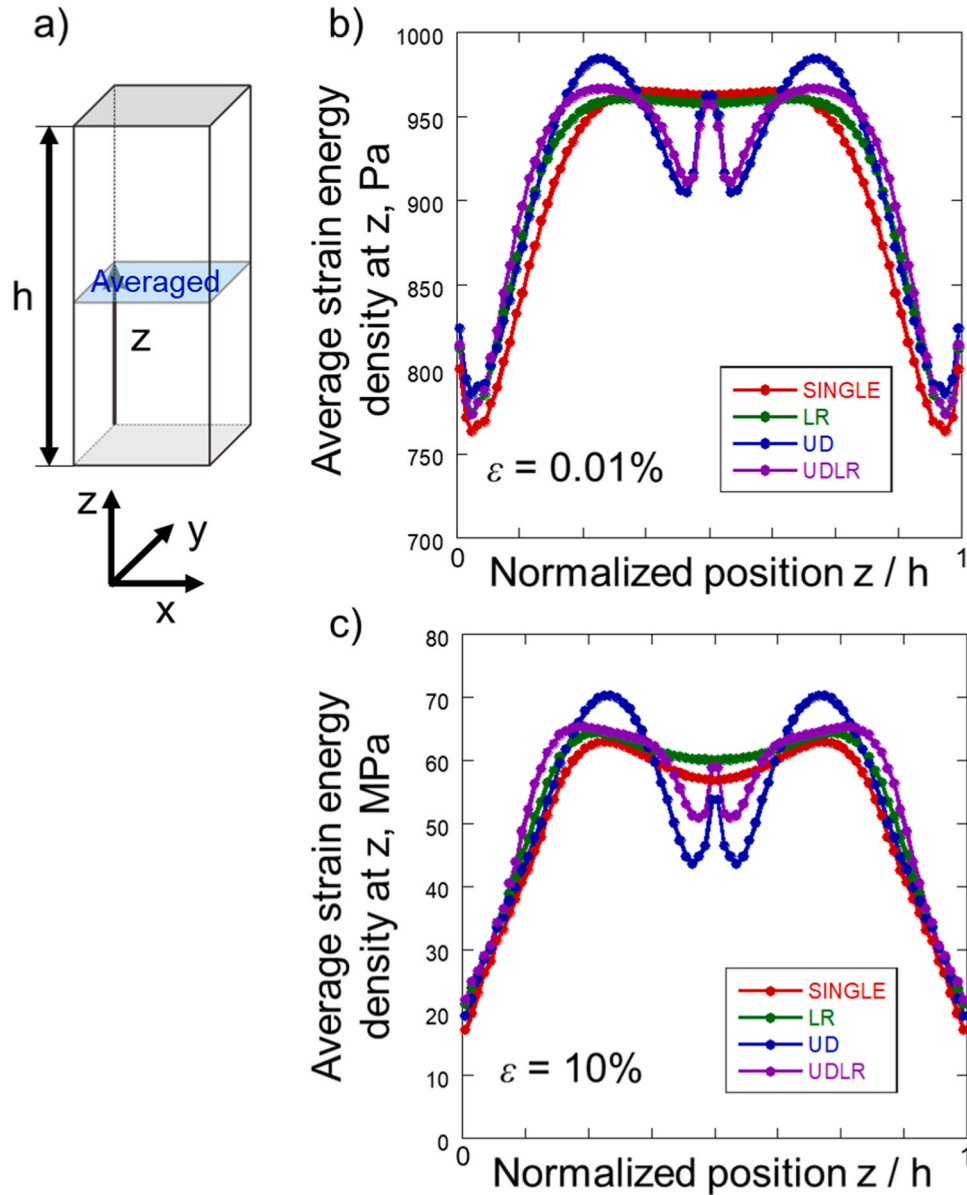

Fig. 10. Calculated strain energy density stored during compression. (a) Averaging value at each z. Relationship between average strain energy density and position z at a compressive strain of (b) 0.01 % and (c) 10 %.
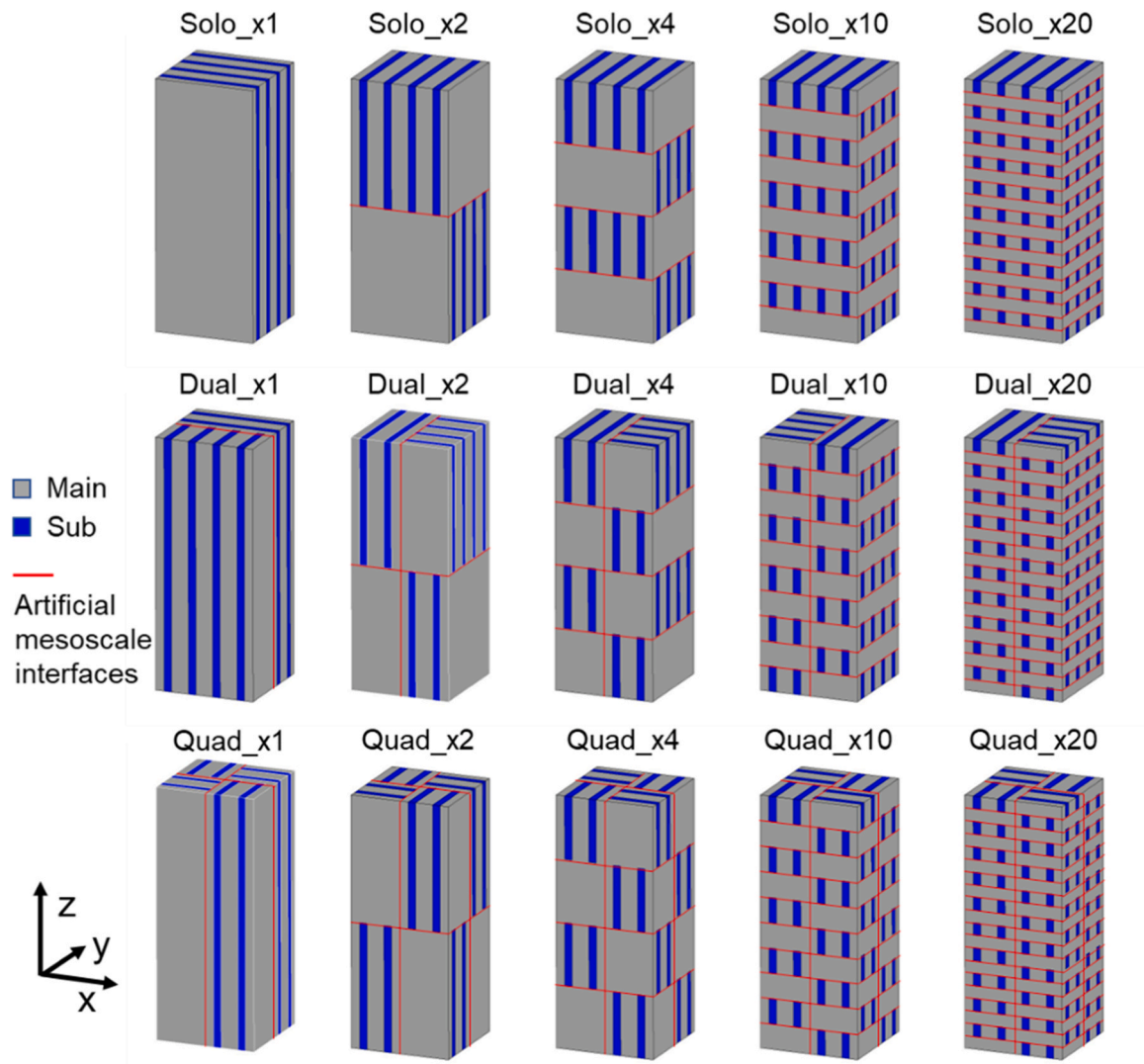
Fig. 11. Typical models of multi-story structures with artificial interfaces.

depending on the structure, as shown in Table 6. During the numerical analysis for this study, all models are subjected to displacement on the top surface. Therefore, the force applied to the deformed model can be derived by dividing the total strain energy by the displacement. In other words, the difference in the mechanical properties depending on the structure, as described in Table 6 and Figs. 7 and 8, can be related to the strain energy stored during deformation. The strain energy was calculated via Gaussian integration of the scalar product of the stress tensor and strain tensor at all integration points in the finite element models.

Table 7 lists the total strain energy calculated for each model during compression to 0.01 and 10 %. As anticipated, the SINGLE model shows the smallest total strain energy compared with other models, thereby explaining the smallest Young's modulus, 0.2 % proof stress, and strain hardening of the SINGLE model compared with those of other models, as shown in Table 6. The difference in total strain energy among UD, LR, and UDLR models is small at 0.01 %, thereby clarifying the small difference in Young's modulus between the UD, LR, and UDLR models. Contrarily, the clear difference in the total strain energy at a compressive strain of 10 % between UD, LR, and UDLR models is attributed to the dissimilarity in the flow stress level, as shown in Fig. 8b. Particularly, the total strain energy values for the SINGLE and UD models are distinctively smaller than those for the LR an UDLR models. This result is consistent with the difference in yield stress (Fig. 8 and Table 6), where the LR and UDLR models exhibit higher yield stress than the SINGLE and UD models.

To better understand the distribution of the stored strain energy, the average strain energy density in the x–y plane at each position z, as shown by the bright blue region in Fig. 10a, is calculated. The average strain energy density as a function of position z at a compressive strain of 0.01 and 10 % is shown in Fig. 10b and c, respectively. Compared to the SINGLE model, the LR model shows a higher energy density, except near the middle of the sample at a compressive strain of 0.01 %. The increase in energy density is attributed to the vertical mesoscale interface between different building blocks, which results in a pronounced increase in the total strain energy of the LR model compared to that of the SINGLE model, as shown in Table 7. The average energy density fluctuates along BD in the UD and UDLR models. Near the middle of the sample (near the horizontal mesoscale interface), the average energy densities of the UD and UDLR models are smaller than that of the SINGLE model. However, a larger energy density in most regions results in a larger total strain energy of the UD and UDLR models, as listed in Table 7. Interestingly, the relationships at a compressive strain of 10 % (Fig. 10c) are qualitatively similar to those at a compressive strain of 0.01 % (Fig. 10b), although the amount of plastic deformation is quite different between the two cases. This difference can probably be attributed to the similarity in the elastic and plastic anisotropies of the present material, as indicated by Fig. 5c and d.
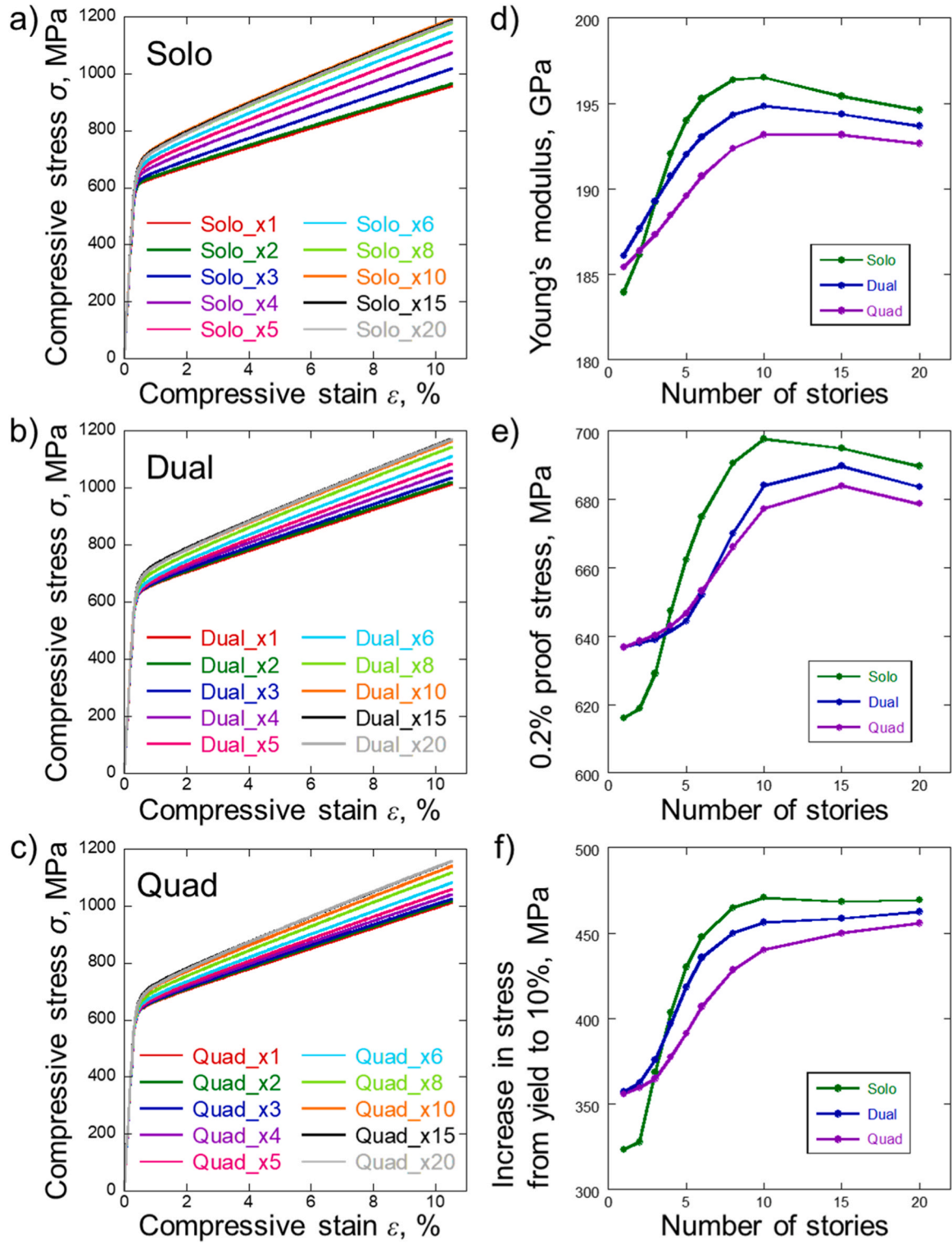
Fig. 12. Possible improvement of mechanical properties. Calculated stress-strain curves for (a) Solo, (b) Dual, and (c) Quad models. Changes in calculated mechanical properties with increase in the number of stories: (d) Young's modulus, (e) 0.2 % proof stress, and (f) increase in stress from yield to 10 %.

4.3. Possible strengthening of multi-story structure

As shown in Table 6 and Figs. 7 and 8, the mesoscale interfaces between the building blocks effectively improve the mechanical properties. Thus, the introduction of more mesoscale interfaces into the material can lead to further improvements in the mechanical properties. In this section, possible strengthening of the AM structure is explored

numerically using systematic calculations.

Schematics of some analysis model examples with different number of mesoscale interfaces are shown in Fig. 11, where the red line indicates the mesoscale interfaces. Solo, Dual, and Quad models contained 0, 1, and 2 mesoscale interfaces in the x–y plane structure, respectively. For each model, ten different models with different numbers of stories (1, 2, 3, 4, 5, 6, 8, 10, 15, and 20) were prepared, and the dimensions of the
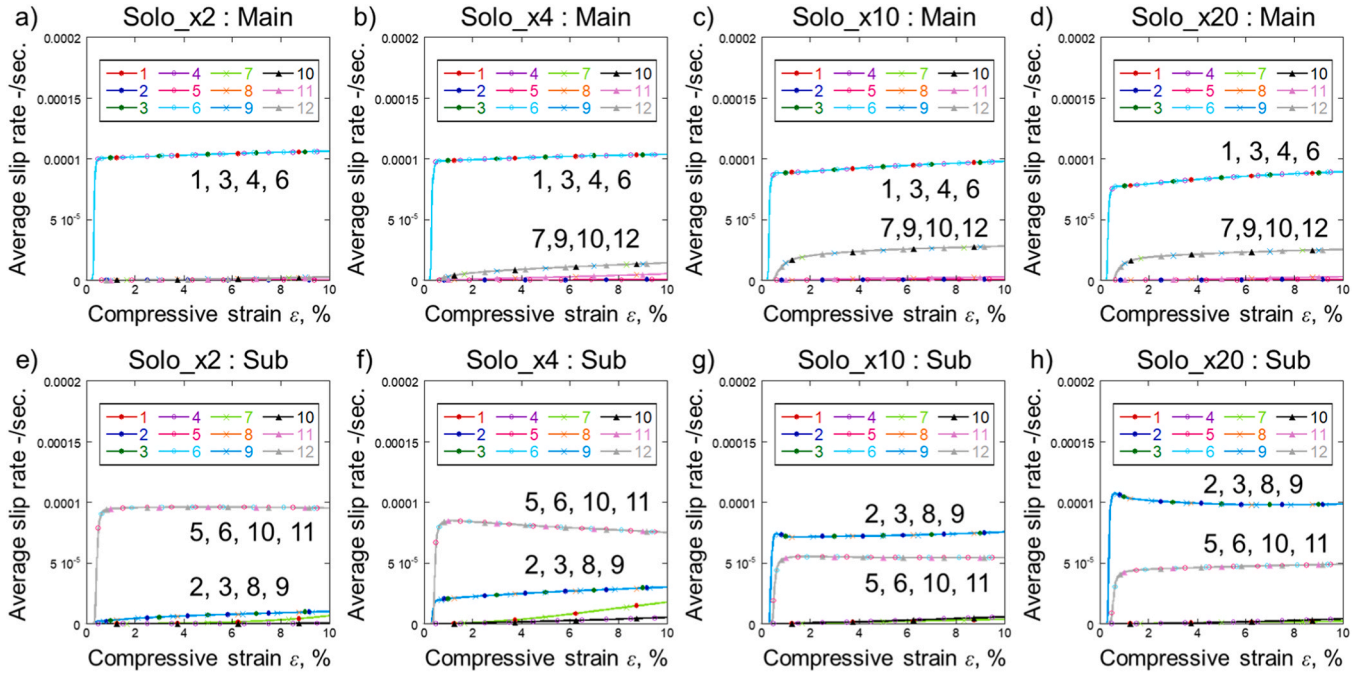
Fig. 13. Calculated activity of slip system in the main layer of (a) Solo_×2, (b) Solo_×4, (c) Solo_×10, and (d) Solo_×20 models; and sub layer of (e) Solo_×2, (f) Solo_×4, (g) Solo_×10, and (h) Solo_×20 models.

models were kept constant at 5×5×12.5 mm. In Fig. 11, the terms ×1, ×2, ×4, ×10, and ×20 indicate the model with 1, 2, 4, 10, and 20 stories, and Solo_×1, Solo_×2, Dual_×1, and Quad_×2 correspond to the SINGLE, UD, LR, and UDLR models of this study, respectively.

The calculated stress–strain curves of the Solo, Dual, and Quad models are shown in Fig. 12a, b, and c, respectively. These results indicate comparisons between models with different number of stories (or different number of mesoscale interfaces). The stress–strain behavior depends on the number of stories in all models. From the obtained results, the dependence of the number of stories on the Young's modulus, 0.2 % proof stress, and increase in stress from yielding to a compressive strain of 10 % is calculated, as shown in Fig. 12d, e, and f. Overall, all values tend to increase with the number of stories to ~10 or 15 stories. On considering Solo models, all values increase from 1 to 10 stories. However, all values slightly decrease from 10 to 20 stories, implying that the mechanical properties of the present AM structure can have an optimum number of stories rather than a monotonic increase. In the case of the Solo model, the optimum number of stories is found to be 10, as shown in Fig. 12d, e, and f. Furthermore, the increases in mechanical properties correlate to total strain energy stored in the structure, similar to Fig. 10 and Table 7. Supplementary Note 6 presents the total strain energy stored in multi-story structures.

The appearance of the optimal number of stories for mechanical properties can be reasonably explained relative to the dependency of the slip system activity on the number of stories. The activities of the slip modes in the main and sub-layers of the Solo models with 2, 4, 10, and 20 stories are shown in Fig. 13. The activity of the main layer of the Solo_x2 model in Fig. 13a indicates that the four equivalent slip systems, 1, 3, 4, and 6, with the same Schmid factor shown in Table 6, are predominantly activated. Slip modes 7, 9, 10, and 12 with a Schmid factor of zero increase the activity (Fig. 13b, c, and d) compared to the negligibly small activity of modes 7, 9, 10, and 12 (Fig. 13a). Additionally, on comparing Fig. 13a, b, c, and d, the activity of slip modes 1, 3, 4, and 6 is found to decrease with an increase in the number of stories. Thus, the contribution of the main layer to the macroscopic compressive deformation decreases with an increase in the number of stories because only slip modes 1, 3, 4, and 6 induce strain in the loading direction. Conversely, the activities of the slip modes in the sub-layer (Fig. 13e, f, g,

and h) show a change in the dominant slip modes from 5, 6, 10, and 11–2, 3, 8, and 9 with an increase in the number of stories. Although slip systems 2, 3, 8, and 9 are suppressed owing to the mechanical interaction between the main and sub-layers, as explained in Section 5.1, the slip systems are enhanced by an increase in the number of stories. Importantly, the contribution of the sub-layer to macroscopic compressive deformation increases because the activity of slip systems 2, 3, 5, 6, 8, 9, 10, and 11 induces strain in the loading direction.

The distributions of ε_{xx} in the Solo_x2 and Solo_x20 models are shown in Fig. 14a where both the x–z surface and the y–z cross-sectional plane are visualized. The schematic in Fig. 14a indicates the visualized regions, where broken lines show the regions removed to visualize the cross-sections. Although no significant difference in ε_{zz} occurs between the main and sub-layers in Solo_x2, compressive strain is much larger in the sub-layer compared to that in the main layer of Solo_x20. Fig. 14b shows the average value of ε_{zz} in the main and sub-layers at a compressive strain of 10 %, as a function of the number of stories in the Solo models. The average values of the strain component ε_{zz} in the main layer and sub-layer were calculated by averaging the total strain component zz at all integration points in main layer and sub-layer, respectively. With an increase in the number of stories, the sub-layer is responsible for a larger compressive strain compared to the main layer, which leads to a decrease in the plastic anisotropy in the lamellar structure because of the larger slip activity of slip systems 2, 3, 8, and 9, which are suppressed in the SINGLE structure. The decrease in plastic anisotropy causes a decrease in the mechanical interaction at the artificially introduced mesoscale interfaces, which results in a decrease in the strength of the AM structure. In conclusion, the optimum number of stories in the AM structure appears owing to the competition between strengthening by mechanical interaction between the building blocks with strong plastic anisotropy and a decrease in the plastic anisotropy of the lamellar structure.

Finally, the mechanism for the appearance of optimum properties is numerically confirmed by additional calculations with the suppression of slip systems 2, 3, 8, and 9 in the sub-layer, as shown in Fig. 14c. The calculated stress–strain curves for the Solo models with the suppression of slip systems 2, 3, 8, and 9 in the sub-layer are shown in Fig. 14d. As the number of stories increases, the stress level increases monotonically.
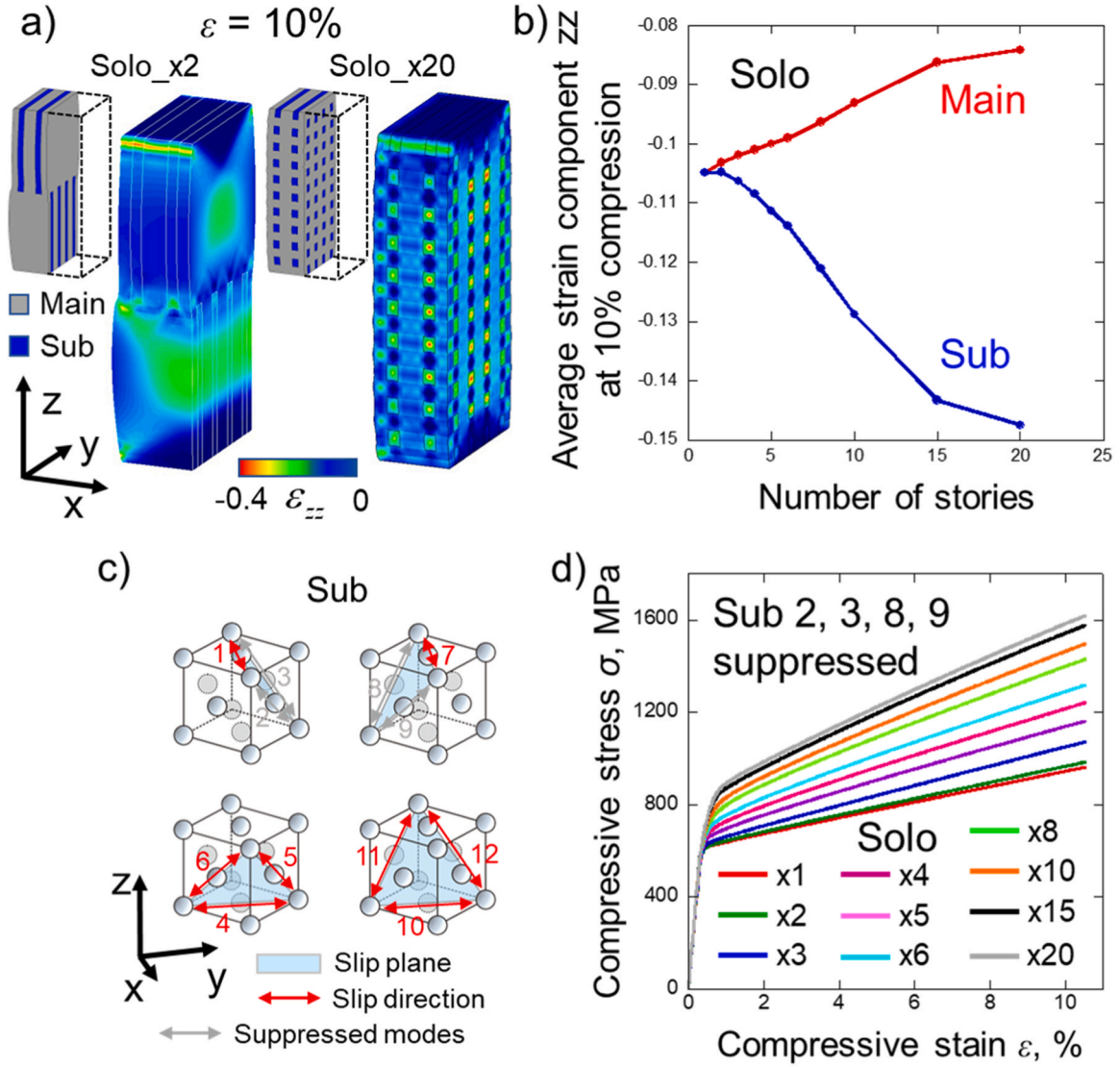
Fig. 14. Contributions of the main and sub layers to compressive deformation and numerical confirmation of influence of plastic relaxation on the sub layer. (a) Calculated distributions of strain component zz (σ_{zz}) in Solo_×2 and Solo_×20 models. (b) Calculated average strain component zz (σ_{zz}) at compressive strain of 10 % in the main and sub layers as a function of number of stories. (c) Suppression of slip mode 2, 3, 8, and 9 in the sub layer. (d) Calculated stress-strain curves of the Solo models with suppression of slip systems 2, 3, 8, and 9 in the sub layer.

The maximum stress at a compressive strain of 10 % in the Solo_x20 model is more than 1600 MPa, which is much larger than the maximum stress of ~1200 MPa for Solo_x10, as shown in Fig. 12a. The suppression of slip systems 2, 3, 8, and 9 in the sub-layer maintains a strong plastic anisotropy of the lamellar structure even for structures with large numbers of stories, leading to a monotonic increase in strength.

5. Conclusions

In this study, we achieved, for the first time, strengthening of IN718 alloy by introducing self-organized microscale lamellar interfaces and artificially introduced mesoscale interfaces into 3D structures via PBF-LB/M AM. The underlying mechanism of the improved mechanical properties and a possible strategy for further strength improvement are explored by numerical analysis based on a crystal plasticity FEM. A summary of the contributions of this study is as follows.

1. Based on the measured elastic constants and crystallographic texture of the strongly oriented AM IN718 alloy fabricated via PBF-LB/M, the elastic stiffness components of an IN718 alloy single crystal exhibiting cubic elastic symmetry are determined as $c_{11} = 223.0$ GPa, $c_{12} = 152.5$ GPa, and $c_{44} = 121.8$ GPa using the iVRH approximation.

2. The experimental results of compressive loading tests for hierarchically structured PBF-LB/M IN718 consist of two building blocks of a lamellar structure with different scanning directions, showing a clear dependence of the yield stress and flow stress levels on the combination and configuration of the building blocks.

3. The underlying deformation mechanism of PBF-LB/M IN718 with hierarchical interfaces is numerically evaluated using crystal plasticity FEM. Self-organized microscale lamellar interfaces between the main and sub-layers induce additional stress owing to elastic and plastic anisotropies that cause the suppression of active slip modes in the sub-layer, resulting in strong plastic anisotropy of the lamellar structure. The plastic anisotropy of the lamellar structure induces mechanical interactions at artificially introduced mesoscale interfaces between the building blocks with different scanning directions. The additional strain energy originating from the mechanical interaction at the mesoscale interfaces increases the macroscopic stress. Consequently, the mechanical properties,

including Young's modulus, 0.2 % proof stress, and strain hardening, are improved by the introduction of mesoscale interfaces.

4. Crystal plasticity analysis of the structure with a larger number of mesoscale interfaces shows better mechanical properties as the total strain energy increases. The numerical results exhibit possible optimum structures relative to the Young's modulus, 0.2 % proof stress, and strain hardening.

5. The appearance of peak properties is due to the competition between an increase caused by mechanical interactions at the mesoscale interfaces between different building blocks and a decrease due to the weakened plastic anisotropy of the building blocks owing to the activation of additional slip modes.

CRediT authorship contribution statement

Tsuyoshi Mayama: Investigation, Methodology, Software, Validation, Visualization, Writing – original draft. **Takuya Ishimoto:** Investigation, Methodology, Visualization, Writing – review & editing. **Masakazu Tane:** Investigation, Methodology, Writing – review & editing. **Ken Cho:** Investigation, Methodology, Writing – review & editing. **Koki Manabe:** Investigation. **Daisuke Miyashita:** Investigation. **Shota Higashino:** Investigation, Methodology. **Taichi Kikukawa:** Investigation. **Hiroyuki Y. Yasuda:** Investigation, Writing – review & editing. **Takayoshi Nakano:** Conceptualization, Project administration, Supervision, Writing – review & editing.

Declaration of Competing Interest

The authors declare that they have no known competing financial interests or personal relationships that could have appeared to influence the work reported in this paper

Data availability

Data will be made available on request.

Acknowledgement

Appendix A. Supporting information

Supplementary data associated with this article can be found in the online version at doi:10.1016/j.addma.2024.104412.

References

[1] I. Gibson, D. Rosen, B. Stucker, M. Khorasani. Additive Manufacturing Technologies, 3rd Ed., Springer, Switzerland, 2021.

[2] J.O. Milewski, Additive Manufacturing of Metals – From Fundamental Technology to Rocket Nozzles, Medical Implants, and Custom Jewelry, in: Springer Series in Materials Science, 258, Springer, Switzerland, 2017.

[3] W.E. Frazier, Metal additive manufacturing: a review, J. Mater. Eng. Perform. 23 (2014) 1917–1928, https://doi.org/10.1007/s11665-014-0958-z.

[4] D. Herzog, V. Seyda, E. Wycisk, C. Emmelmann, Additive manufacturing of metals, Acta Mater. 117 (2016) 371–392, https://doi.org/10.1016/j.actamat.2016.07.019.

[5] T. DebRoy, H.L. Wei, J.S. Zuback, T. Mukherjee, J.W. Elmer, J.O. Milewski, A. M. Beese, A. Wilson-Heid, A. De, W. Zhang, Additive manufacturing of metallic composites – process, structure and properties, Prog. Mater. Sci. 92 (2018) 112–224, https://doi.org/10.1016/j.pmatsci.2017.10.001.

[6] T.D. Ngo, A. Kashani, G. Imbalzano, K.T.Q. Nguyen, D. Hui, Additive manufacturing (3D printing): a review of materials, methods, applications and challenges, Compos. Part B 143 (2018) 172–196, https://doi.org/10.1016/j.compositesb.2018.02.012.

[7] T. Ishimoto, K. Hagihara, K. Hisamoto, S.-H. Sun, T. Nakano, Crystallographic texture control of beta-type Ti-15Mo-5Zr-3Al alloy by selective laser melting for the development of novel implants with a biocompatible low Young's modulus, Scr. Mater. 132 (2017) 34–38, https://doi.org/10.1016/j.scriptamat.2016.12.038.

[8] R.W. Messler, Principles of Welding, Wiley, New York, 2008.

[9] T. Ishimoto, K. Hagihara, K. Hisamoto, T. Nakano, Stability of crystallographic texture in laser powder bed fusion: understanding the competition of crystal growth using a single crystalline seed, Addit. Manuf. 43 (2021) 102004, https://doi.org/10.1016/j.addma.2021.102004.

[10] K. Hagihara, T. Nakano, Control of anisotropic crystallographic texture in powder bed fusion additive manufacturing of metals and ceramics – a review, JOM 74 (2022) 1760–1773, https://doi.org/10.1007/s11837-021-04966-7.

[11] J.D. Livingston, B. Chalmers, Multiple slip in bicrystal deformation, Acta Metall. 5 (1957) 322–327, https://doi.org/10.1016/0001-6160(57)90044-5.

[12] J.P. Hirth, The influence of grain boundaries on mechanical properties, Metall. Trans. 3 (1972) 3047–3067, https://doi.org/10.1007/BF02661312.

[13] T. Mayama, T. Ohashi, R. Kondou, Geometrically necessary dislocation structure organization in FCC bicrystal subjected to cyclic plasticity, Int. J. Plast. 25 (2009) 2122–2140, https://doi.org/10.1016/j.ijplas.2009.02.001.

[14] T. Ohashi, R. Kondou, Evolution of dislocation pattern in a tricrystal model subjected to cyclic loading, Philos. Mag. 93 (2013) 366–387, https://doi.org/10.1080/14786435.2012.721017.

[15] Y. Kawano, T. Ohashi, T. Mayama, R. Kondou, Crystal plasticity analysis of change in incompatibility and activities of slip systems in α-phase of Ti alloy under cyclic loading, Int. J. Mech. Sci. 146–147 (2018) 475–485, https://doi.org/10.1016/j.ijmecsci.2017.09.023.

[16] Z. Zhao, M. Ramesh, D. Raabe, A.M. Cutiño, R. Radovitzky, Investigation of three-dimensional aspects of grain-scale plastic surface deformation of an aluminum oligocrystal, Int. J. Plast. 24 (2008) 2278–2297, https://doi.org/10.1016/j.ijplas.2008.01.002.

[17] Y. Guan, B. Chen, J. Zou, T.B. Britton, J. Jiang, F.P.E. Dunne, Crystal plasticity modelling and HR-DIC measurement of slip activation and strain localization in single and oligo-crystal Ni alloys under fatigue, Int. J. Plast. 88 (2017) 70–88, https://doi.org/10.1016/j.ijplas.2016.10.001.

[18] E. Demir, I. Gutierrez-Urrutia, Investigation of strain hardening near grain boundaries of an aluminum oligocrystal: experiments and crystal based finite element method, Int. J. Plast. 136 (2021) 102898, https://doi.org/10.1016/j.ijplas.2020.102898.

[19] J.M. Hestroffer, M.I. Latypov, J.-C. Stinville, M.-A. Charpagne, V. Valle, M. P. Miller, T.M. Pollock, I.J. Beyerlein, Development of grain-scale slip activity and lattice rotation fields in Inconel 718, Acta Mater. 226 (2022) 117627, https://doi.org/10.1016/j.actamat.2022.117627.

[20] R.S. Davis, R.L. Fleischer, J.D. Livingston, B. Chalmers, Effect of orientation on the plastic deformation of aluminum single crystals and bicrystals, Trans. AIME 209 (1957) 136–140.

[21] T. Takasugi, N. Fat-Halla, O. Izumi, The plastic deformation and fracture behaviors of α–β brass two-phase bicrystals, Acta Metall. 26 (1978) 1453–1459, https://doi.org/10.1016/0001-6160(78)90160-8.

[22] O. Gokcekaya, T. Ishimoto, S. Hibino, J. Yasutomi, T. Narushima, T. Nakano, Unique crystallographic texture formation in Inconel 718 by laser powder bed fusion and its effect on mechanical anisotropy, Acta Mater. 212 (2021) 116876, https://doi.org/10.1016/j.actamat.2021.116876.

[23] A. Panesar, M. Abdi, D. Hickman, I. Ashcroft, Strategies for functionally graded lattice structures derived using topology optimization for additive manufacturing, Addit. Manuf. 19 (2018) 81–94, https://doi.org/10.1016/j.addma.2017.11.008.

[24] B. Rankouhi, K.M. Bertsch, G.M. de Bellefon, M. Thevamaran, D.J. Thoma, K. Suresh, Experimental validation and microstructure characterization of topology optimized, additively manufactured SS316L components, Mater. Sci. Eng. A 776 (2020) 139050, https://doi.org/10.1016/j.msea.2020.139050.

[25] D. Li, W. Liao, N. Dai, G. Dong, Y. Tang, Y.M. Xie, Optimal design and modeling of gyroid-based functionally graded cellular structures for additive manufacturing, Comput. -Aided Des. 104 (2018) 87–99, https://doi.org/10.1016/j.cad.2018.06.003.

[26] D. Peirce, R.J. Asaro, A. Needleman, Material rate dependence and localized deformation in crystalline solids, Acta Metall. 31 (1983) 1951–1976, https://doi.org/10.1016/0001-6160(83)90014-7.

[27] F. Roters, P. Eisenlohr, L. Hantcherli, D.D. Tjahjanto, T.R. Bieler, D. Raabe, Overview of constitutive laws, kinematics, homogenization and multiscale

methods in crystal plasticity finite-element modeling: theory, experiments, applications, Acta Mater. 58 (2010) 1152–1211, https://doi.org/10.1016/j.actamat.2009.10.058.

[28] I. Ohno, Free vibration of a rectangular parallelepiped crystal and its application to determination of elastic constants of orthorhombic crystals, J. Phys. Earth 24 (1976) 355–379, https://doi.org/10.4294/jpe1952.24.355.

[29] H. Ogi, K. Sato, T. Asada, M. Hirao, Complete mode identification for resonance ultrasound spectroscopy, J. Acoust. Soc. Am. 112 (2002) 2553–2557, https://doi.org/10.1121/1.1512700.

[30] M. Tane, Y. Nagai, H. Kimizuka, K. Hagihara, Y. Kawamura, Elastic properties of Mg-Zn-Y alloy single crystal with a long-period stacking-ordered structure, Acta Mater. 61 (2013) 6338–6351, https://doi.org/10.1016/j.actamat.2013.06.041.

[31] M. Tane, K. Yamori, T. Sekino, T. Mayama, Impact of grain shape on the micromechanics-based extraction of single-crystalline elastic constants from polycrystalline samples with crystallographic texture, Acta Mater. 122 (2017) 236–251, https://doi.org/10.1016/j.actamat.2016.09.040.

[32] G. Martin, N. Ochoa, K. Saï, E. Hervé-Luanco, G. Cailletaud, A multiscale model for the elastoviscoplastic behavior of directionally solidified alloys: application to FE structural computations, Int. J. Solids Struct. 51 (2014) 1175–1187, https://doi.org/10.1016/j.ijsolstr.2013.12.013.

[33] S. Jothi, S.V. Merzlikin, T.N. Croft, J. Andersson, S.G.R. Brown, An investigation of micro-mechanisms in hydrogen induced cracking in nickel-based superalloy 718, J. Alloy. Compd. 664 (2016) 664–681, https://doi.org/10.1016/j.jallcom.2016.01.033.

[34] C. Kumara, D. Deng, J. Moverare, P. Nylén, Modelling of anisotropic elastic properties in alloy 718 built by electron beam melting, Mater. Sci. Technol. 34 (2018) 529–537, https://doi.org/10.1080/02670836.2018.1426258.

[35] R.E. Newnham, Properties of Materials, Oxford University Press, New York, 2005.

[36] G.M. Volpato, U. Tetzlaff, M.C. Fredel, A comprehensive literature review on laser powder bed fusion of Inconel superalloys, Addit. Manuf. 55 (2022) 102871, https://doi.org/10.1016/j.addma.2022.102871.